ACS APPLIED ELECTRONIC MATERIALS

Article

Cite This: ACS Appl. Electron. Mater. 2019, 1, 2646−2654

pubs.acs.org/acsaelm

Engineering the Interfacial Electronic Structure of Epitaxial Ge/AlAs(001) Heterointerfaces via Substitutional Boron Incorporation: The Roles of Doping and Interface Stoichiometry

Michael B. Clavel,[†] Gabriel Greene-Diniz,[‡] Myrta Grüning,[‡,§] Karen T. Henry,[∥] Markus Kuhn,[∥] Robert J. Bodnar,[⊥] and Mantu K. Hudait*[,†]

[†]Advanced Devices and Sustainable Energy Laboratory (ADSEL), Bradley Department of Electrical and Computer Engineering, Virginia Tech, Blacksburg, Virginia 24061, United States

[‡]School of Mathematics and Physics, Queen's University Belfast, Belfast BT7 1NN, Northern Ireland, United Kingdom

[§]European Theoretical Spectroscopy Facility (ETSF), B-4000 Liège, Belgium

[∥]Intel Corporation, Hillsboro, Oregon 97124, United States

[⊥]Fluids Research Laboratory, Department of Geosciences, Virginia Tech, Blacksburg, Virginia 24061, United States

Supporting Information

ABSTRACT: A joint experimental and theoretical framework for the decoupling of boron (B) doping and stoichiometric-induced modifications to the structural properties and electronic band structure of germanium (Ge)/AlAs(001) heterostructures is presented. The effect of B-induced stress on nearest-neighbor Ge bonds is quantified via X-ray diffractometry and Raman spectroscopic analysis and subsequently interpreted through the lens of density functional perturbation theory. Similarly, experimental determination of the energy band alignment at the *p*-type Ge:B/AlAs heterointerface is understood using a density functional theory approach to model the influence of heterointerface stoichiometry and interatomic bonding between group IV and III−V interfacial atoms on the valence and conduction band discontinuities. The modeled two monolayer interatomic diffusion at the Ge/AlAs heterointerface is confirmed via atom probe tomography analysis, demonstrating a ∼6 Å interfacial width. These results present a unified picture of the Ge:B/AlAs(001) material system, highlighting the influence of B on its structural and electronic properties, and provide a path for the engineering of such heterointerfaces through high concentration dopant incorporation within the overlying Ge epilayer.

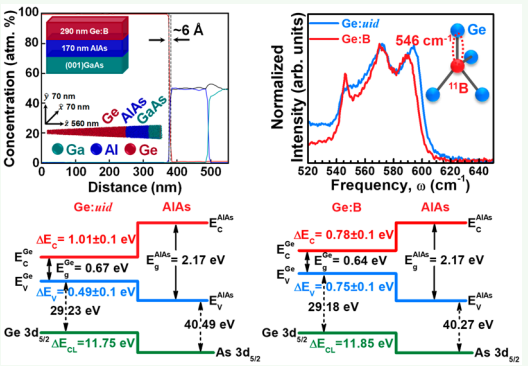

KEYWORDS: *germanium, AlAs, band alignment, molecular beam epitaxy, X-ray photoelectron spectroscopy, Raman spectroscopy, first-principles, density functional theory*

INTRODUCTION

The high concentration *in situ* or *ex situ* doping of $Si_{1-x}Ge_x$ and Ge thin films has attracted significant research interest recently due to its wide ranging applications in state-of-the-art complementary metal-oxide-semiconductor (CMOS) technology,[1−3] monolithically integrated photonic and optoelectronic devices on Si,[4−7] and spintronics.[8,9] Although significant effort has been devoted toward achieving heavily doped $Si_{1-x}Ge_x$[10] and Ge[11−13] materials exhibiting monocrystalline structure,[14,15] high dopant activation levels,[16,17] and low surface roughness,[18] little to no attention has been given to the origin of the B-induced Ge crystal distortion that has been repeatedly observed in practice. Moreover, as complex heterostructures become increasingly desirable in future device technologies owing to their unique electronic and optical properties,[19] the integration of intrinsic and doped Ge thin films on multiple substrate platforms will be essential. Of particular interest for the development of next-generation, Ge-based CMOS devices is the integration of Ge thin films on large bandgap materials such as amorphous insulators (i.e., GeOI)[20,21] or crystalline, Al-bearing III−V alloys.[22−25] Consequently, understanding the impacts of (i) incorporating dopants at high concentrations and (ii) the heterointerface atomic bonding environment (e.g., Ge bound to group III vs. group IV species) on the interfacial electronic structure of such heterostructures are of equal importance.

In this work, we employ a joint experimental and theoretical approach to show that the effect of B incorporation in Ge at high concentration ($N_B \approx 2-4 \times 10^{19}$ cm^{-3}, as measured via Hall analysis) is to introduce a net tensile strain within the Ge

Received: September 19, 2019
Accepted: November 11, 2019
Published: November 11, 2019

DOI: 10.1021/acsaelm.9b00615
ACS Appl. Electron. Mater. 2019, 1, 2646−2654

crystal. The origin of the B-induced strain stems from the significant difference in bond length between the Ge−Ge and Ge−B bonds, the latter of which causes a net elongation of the former, generating the observed in-plane biaxial tensile stress. Moreover, we empirically demonstrate an increase (decrease) in the Ge/AlAs(001) heterointerfacial valence (conduction) band offset of 0.26 eV (0.23 eV), the asymmetry of which results from the coupled effects of the change in the Ge:B quasi Fermi level and the alteration of the Ge band structure due to the B-induced tensile strain. Subsequently, we discuss the effects of heterointerface bonding configurations on the empirical energy band discontinuities as modeled using density functional theory, explicitly taking into consideration the 3d semicore energy levels utilized experimentally. Additionally, modeling of the interatomic diffusion is independently validated using atom probe tomography three-dimensional ion mapping of representative Ge:B/AlAs heterointerfaces.

RESULTS AND DISCUSSION

Structural Characterization of the Ge:*uid*/AlAs(001) and Ge:B/AlAs(001) Heterostructures. Recent computational results[26] indicate that the Ge bonding environment in Ge/III−V heterostructures (i.e., Ge bound to group III or group V atoms at the interface) plays a critical role in the determination of the heterointerfacial electronic structure. Consequently, determining the extent to which atomic interdiffusion occurs, and thereby its likelihood of distorting the ideal (stoichiometric) Ge/III−V interface, becomes necessary when attempting to probe its energy band structure. To this end, we investigated the heterointerface abruptness between the Ge epilayer and underlying III−V substrate using atom probe tomography (APT). The bottom-left inset of Figure 1 highlights the reconstructed three-dimensional (3-D)

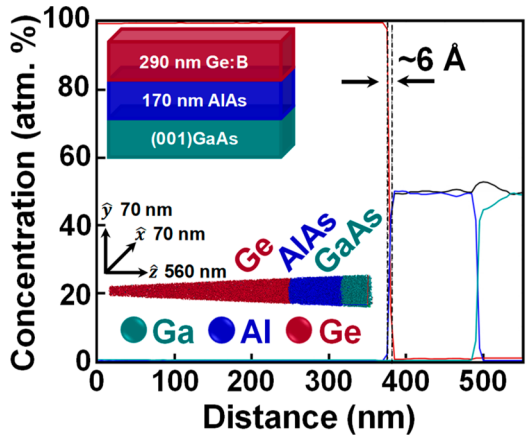

Figure 1. Calculated compositional profile of the reconstructed 3-D ion map depicted by the bottom-left inset (70 × 70 × 560 nm volume). Top-left inset shows a cross-sectional structural schematic of the nominal Ge:B/AlAs/GaAs(001) heterostructure investigated herein. A ~6 Å Ge:B/AlAs interfacial width was observed.

ion map of a 70 × 70 × 560 nm (conical) volume taken from a representative Ge:B/AlAs/GaAs(001) heterostructure, nominally depicted in the top-left inset of Figure 1. Using these data, a compositional depth profile (Figure 1) was generated, by which the atomic interdiffusion at each heterointerface was estimated by measuring the separation between the 90 and 10% atomic thresholds for a given ion species. From Figure 1, the heterointerface abruptness at the Ge:B/AlAs interface was found to be ~6 Å, indicating that no quantifiable atomic interdiffusion occurred beyond an initial two monolayer (ML) diffuse region formed at the onset of Ge nucleation. This result is partly explained by the low-temperature Ge epitaxy conditions used herein (see Materials and Methods), which serve to minimize As desorption from the AlAs surface prior to and during initial Ge nucleation. It should be noted that such As surface desorption would concomitantly leave the AlAs surface Al (group III)-rich, thereby directly impacting the heterointerfacial electronic structure.[26] Moreover, the low Ge growth rate utilized promotes uniform Ge surface coverage and Frank−van der Merwe-dominated growth. Taken in tandem, the net effect of these two processes is to reduce the likelihood of As out-diffusion into the growing Ge epilayer, thereby maintaining a more stoichiometric AlAs surface as well as preserve heterointerfacial abruptness, as demonstrated in Figure 1.

We next studied the impact of B dopant incorporation on the structural characteristics of Ge/AlAs/GaAs(001) heterostructures, including Ge epilayer crystallinity and strain-state. Figure 2a depicts the measured ω-2θ high-resolution X-ray diffraction (HR-XRD) spectra, taken along the symmetric (004) direction, for the as-grown Ge:*uid*/AlAs/GaAs(001) (blue) and Ge:B/AlAs/GaAs(001) (red) heterostructures. Due to the selected measurement orientation, a direct, albeit qualitative, correlation between residual film stresses and the Bragg angle of a given epilayer can be established. Specifically, in-plane biaxial tension (compression) would be observed as an increase (decrease) in the measured (004) epilayer Bragg angle, i.e., the angle corresponding to the out-of-plane lattice constant, $a_\perp$, of the film. This can be interpreted as a resulting contraction (expansion) of $a_\perp$ due to the applied in-plane stress and the necessary volume conservation requirement of the crystal's unit cell. As can be seen in Figure 2a, an upshift in the Ge Bragg angle was indeed observed for the Ge:B/AlAs/GaAs(001) heterostructure, as compared to the Ge:*uid*/AlAs/GaAs(001) material system, indicating the presence of residual in-plane tensile strain in the Ge:B epilayer that was not detected in the *uid* Ge film.

Quantification of the Ge strain-state induced by the high B concentration was performed by way of symmetric (004) and asymmetric (115) reciprocal space mapping, as shown in Figures 2b and 2c, respectively. We note that only the centroid of each epilayer's reciprocal lattice point (RLP), as indicated in Figures 2b and 2c, was used throughout the strain relaxation analysis, thereby minimizing errors introduced by the high-degree of convolution (minimal lattice spacing differentiation) between the Ge, AlAs, and GaAs diffraction contours. Following the detailed procedures outlined in refs 27−30 and assuming a relaxed, cubic Ge lattice constant value of 5.658 Å,[31] the measured, B-induced Ge in-plane tensile strain was found to be 0.25 ± 0.06%. Moreover, as can be seen in Figures 2b and 2c, despite the added tensile stress due to B incorporation, no measurable lattice tilting, mosaicity, or broadening of the Ge RLP was observed, indicating the preservation of film crystallinity between the *uid* and B-doped heterostructures. This is in contrast to previous investigations,[14,32] wherein measurable surface roughening and polycrystalline epilayer growth were observed in Si and Ge films, attributable to B surface segregation and/or film relaxation during growth. Such plastic relaxation would be expected to occur in a strained epilayer whose thickness exceeds the critical layer thickness, at which point defect

DOI: 10.1021/acsaelm.9b00615
ACS Appl. Electron. Mater. 2019, 1, 2646−2654

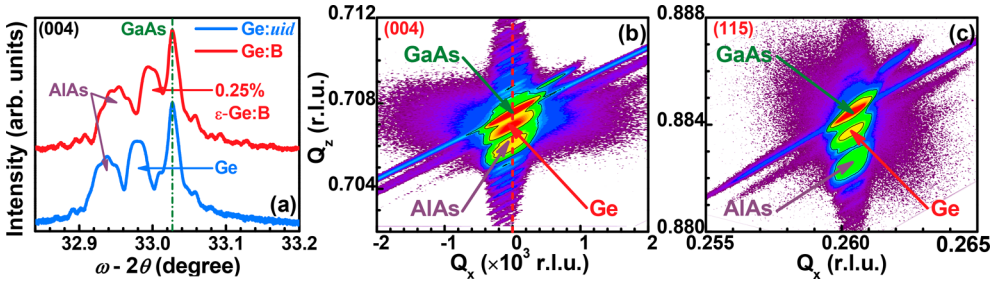

Figure 2. (a) Symmetric (004) rocking curve of the Ge:*uid*/AlAs/GaAs(001) (blue) and Ge:B/AlAs/GaAs(001) (red) heterostructures highlighting the increase in the Ge Bragg angle due to tensile stress within the Ge film. (b) Symmetric (004) and (c) asymmetric (115) reciprocal space maps of the Ge:B/AlAs/GaAs(001) heterostructure, from which a tensile strain of 0.25 ± 0.06% within the Ge:B epilayer was extracted.

nucleation becomes feasible under the energy balanced model proposed in ref.[33]

The strain-state of the epitaxial Ge:B layer was independently corroborated via analysis of Raman spectra that were recorded from the surface of both as-grown heterostructures, as shown in Figure 3a. With respect to the unstrained Ge−Ge

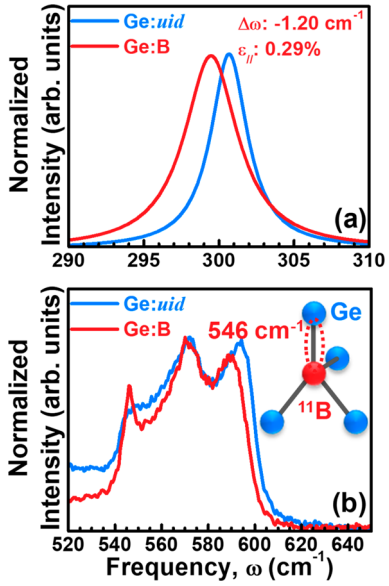

Figure 3. (a) Fitted Raman spectra of the Ge:*uid* (blue) and Ge:B (red) epitaxial thin films grown on AlAs/GaAs(001). The measured wavenumber shift of −1.20 cm^{-1} corresponds to an in-plane, biaxial tensile strain of 0.29 ± 0.05% within the highly B-doped Ge epilayer. (b) Raman spectral signature of the B−Ge bond located at $\omega \sim 546$ cm^{-1} (red) as well as its absence from the recorded Ge:*uid* spectra (blue).

longitudinal optical (LO) phonon mode located at ∼300 cm^{-1}, the Ge:B film exhibited a wavenumber shift, $\Delta\omega$, of −1.20 cm^{-1}. Employing the previously reported[28,34] relation $\Delta\omega = -b\varepsilon_{\parallel}$, where $\Delta\omega$ is the wavenumber shift (in cm^{-1}) and b is a material parameter dependent on the material's elastic constants and vibrational properties, the empirical material strain-state, $\varepsilon_{\parallel}$, can be correlated with its measured Raman wavenumber shift. Using the literature reported value of b = 415 cm^{-1} for Ge,[28,35] the Raman-deduced Ge:B epilayer strain was found to be 0.29 ± 0.05%, in excellent agreement with the Ge:B strain-state as determined via X-ray diffraction analysis. We note that although a splitting of the fundamental phonon modes in the presence of strain is expected, the magnitude of said strain-induced separation is below measurement sensitivity limits, as will be expanded upon theoretically in the following section. Moreover, additional evidence for the successful incorporation of B into the Ge film can be provided by identification of the local vibrational mode (LVM) associated with the Ge−B bond within the measured Raman spectra.[36] As can be seen in Figure 3b, the Ge−B LVM was indeed observed at ∼546 cm^{-1} within the measured Ge:B Raman spectra (red), in contrast to the Ge:*uid* spectra (blue), which lacks this distinct spectral signature.

Origin of Lattice Contraction in the Ge:B/AlAs(001) System. To validate the above empirical results within a theoretical framework, *ab initio* atomistic density functional perturbation theory (DFPT) calculations were used to evaluate the effects of strain and B incorporation within the Ge lattice on its vibrational properties. Figure 4a (top) depicts the calculated phonon dispersions curves for unstrained (black) and 0.29% biaxial tensile strained (red) undoped Ge, whereas Figure 4a (bottom) presents a magnified view of the same within the vicinity of the Γ-point. As can be seen in Figure 4a, biaxial tensile strain results in a splitting and downward shift of the fundamental LO mode(s) at the Γ-point due to a reduction in crystal symmetry. This is quantitatively presented in Table 1, wherein a range of biaxial tensile strain (ε) values was investigated and their corresponding downshift (and thereby separation) with respect to unstrained Ge are tabulated. As indicated in Table 1, for an expected strain of 0.29%, the corresponding predicted downshift in the LO phonon mode(s) is −1.21 and −1.42 cm^{-1} with the difference (0.21 cm^{-1}) being the magnitude of the strain-induced mode splitting. These results are in excellent agreement with the measured Raman wavenumber shift, $\Delta\omega$ = 1.20 cm^{-1}, corresponding to an experimental Ge strain-state of 0.29%, as highlighted in Figure 3a. Moreover, the calculated downshifts in phonon frequency reaffirm the previously stated supposition that the magnitude of the strain-induced LO mode splitting is insufficiently large to be quantified experimentally.

The LVM corresponding to B_{Ge} were also calculated as a function of decreasing B concentration, achieved through increasing simulation cell volume while maintaining one B dopant atom per cell. Smaller cell sizes correspond to strong elastic interactions between periodic images of the B_{Ge} dopant, which vanish in the dilute limit. The B_{Ge} LVM frequency converges from below as a function of cell volume; hence, the elastic interactions between neighboring dopants tend to soften their vibrational modes. Figure 4b depicts the B_{Ge} oscillation mode parallel to the ⟨100⟩ direction as a function of increasing simulation cell volume (decreasing B concentration). A value of 557 cm^{-1} was obtained for the largest simulation cell, which corresponded to a B concentration of

DOI: 10.1021/acsaelm.9b00615
ACS Appl. Electron. Mater. 2019, 1, 2646−2654

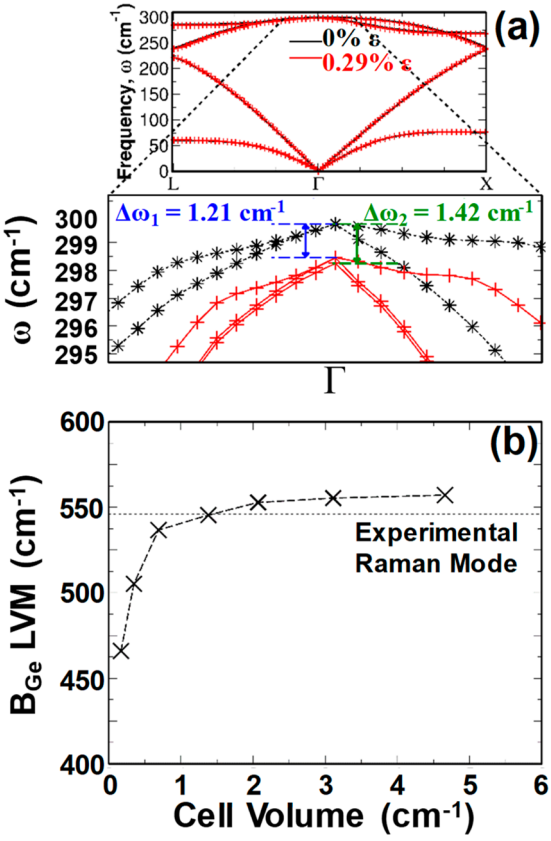

Figure 4. (a) Phonon dispersion curves calculated using DFPT for biaxially strained, undoped Ge. The magnified region highlights the calculated downshift (and split) of the phonon dispersion near the Γ-point resulting from the incorporation of 0.29% strain. (b) Local vibrational modes for B_{Ge} as a function of decreasing B concentration (increasing cell volume).

Table 1. Calculated Splitting and Shift of the Fundamental Mode of Ge (in cm^{-1}) as a Function of Biaxial Strain

strain, ε (%)	$\Delta\omega_1$	$\Delta\omega_2$
0.0	0	0
0.1	−0.54	−0.59
0.15	−0.65	−0.75
0.25	−0.85	−0.99
0.28	−1.18	−1.32
0.29	−1.21	−1.42
0.30	−1.26	−1.46

~2.1 × 10^{20} cm^{-1}. Given the importance of effects not accounted for here, such as the random distribution of dopants in physical samples, the interaction of B with other unintentional dopants, and the temperature dependence of the vibrational modes, the calculated LVM frequency is considered to agree reasonably well with the experimental, Raman-deduced result of 546 cm^{-1} shown in Figure 3b. Moreover, the overestimation of the calculated LVM frequency is also consistent with the tendency of LDA to overbind atoms.

Whereas the previous results establish the level of accuracy of the employed methods (with respect to experiment) for the vibrational properties of B-doped Ge, the vibrational density of states (VDOS) of undoped and B-doped Ge were also calculated to investigate the dependence of Ge vibrational modes on B dopant concentration. These results are shown in Figures 5a–d for undoped Ge, and Ge:B simulation cells consisting of 32, 16, and 8 atoms, respectively, corresponding

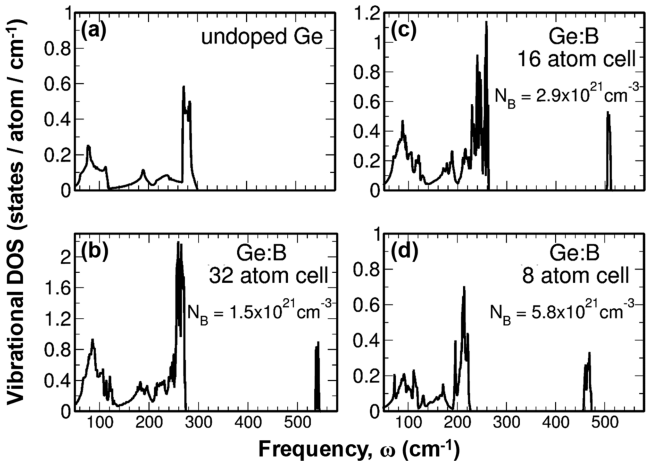

Figure 5. Vibrational density of states calculated for (a) undoped Ge, (b) $N_B \sim 1.5 \times 10^{21}$ cm^{-3}, (c) $N_B \sim 2.9 \times 10^{21}$ cm^{-3}, and (d) $N_B \sim 5.8 \times 10^{21}$ cm^{-3}. The decrease in fundamental phonon mode frequencies observed as N_B increases mirrors the expected decrease in phonon frequencies correlated with increasing tensile strain, implying a direct relationship between B concentration and the residual tensile stress present in highly doped Ge:B.

to B concentrations (N_B) of ~1.5 × 10^{21} cm^{-3}, ~2.9 × 10^{21} cm^{-3}, and ~5.8 × 10^{21} cm^{-3}. Given that elastic tensile strain tends to decrease the frequency of fundamental phonon modes (cf. Figure 4a and Table 1), the observed reduction in frequency of the calculated modes (relative to undoped Ge, $\omega_0 \sim 300$ cm^{-1}) is consistent with increasing tensile strain within Ge as B concentration increases. We note that due to the large computational cost of VDOS calculations in nonprimitive cells (in particular, the summations over irreducible representations of atomic displacements defined by the grid of q-points), the calculations presented here have been restricted to smaller simulation cells, thereby corresponding to very high concentrations of B. However, despite this, the qualitative relationship observed between B dopant concentration and Ge phonon modes depicted in Figure 5 remains clear: increasing B concentration results in decreasing Ge phonon frequencies, as one might expect for increasing tensile strain. In accordance with the previously discussed experimental results, the presented simulation results reaffirm the creation of an effective tensile strain within Ge induced by elevated B dopant concentrations. This strain stems from a combination of the large mismatch between Ge–Ge and Ge–B bond lengths[44] and the presence of the underlying substrate, which prevents relaxation of the Ge lattice in the vicinity of the dopant atom. Given that the Ge lattice is "fixed" to that of the III–V substrate, the shortening of nearest-neighbor Ge–B bonds leads to a net elongation of the surrounding Ge–Ge bonds, following the assumption that B atoms are distributed roughly homogeneously throughout the Ge film. This effect is graphically represented in Figure S1, which shows a representative Ge:B supercell containing a singular substitutional B impurity atom and its modeled effect on local bond lengths within the vicinity of the B impurity (see Figure S1b). A similar, quantitative depiction can be found in Figure S2, which demonstrates the impact of increasing B dopant concentration on the volume expansion (and thus stress) of

DOI: 10.1021/acsaelm.9b00615
ACS Appl. Electron. Mater. 2019, 1, 2646–2654

nearby Ge unit cells, thereby providing a secondary perspective in which to relate increasing B dopant density to increasing tensile strain within the Ge film.

Empirical and Computational Ge:*uid*/AlAs and Ge:B/AlAs Heterointerface Energy Band Structures. Figure 6 shows representative X-ray photoelectron spectroscopy (XPS) spectra used in the determination of the energy band alignment at the Ge/AlAs heterointerface for the (Figures 6a−c) Ge:*uid*/AlAs(001), and (Figures 6d−f) Ge:B/AlAs(001) heterostructures. To this end, three distinct surfaces were analyzed, including: (i) 270 nm (290 nm), bulk-like Ge as-grown (either *uid* or B-doped) on AlAs/GaAs(001); (ii) bulk-like AlAs as-grown on GaAs(001); and (iii) photoelectron-transparent, ultrathin (~1.5 nm) Ge as-grown on AlAs/GaAs(001). The photoelectron transparency requirement stipulated in (iii) allows for direct measurement of both Ge- and As-originating interfacial core level (CL) binding energies (BEs) precisely at the Ge/AlAs heterointerface. Following the well-established[27,28,37] methodology of Kraut et al.,[38] the heterointerface valence band offset (ΔE_V) can be expressed as,

$$\Delta E_V = (E^{Ge}_{Ge3d_{5/2}} - E^{Ge}_{VBM}) - (E^{AlAs}_{As3d_{5/2}} - E^{AlAs}_{VBM}) + (E^{Ge}_{Ge3d_{5/2}}(i) - E^{AlAs}_{As3d_{5/2}}(i)) \quad (1)$$

where $E^{Ge}_{Ge\ 3d_{5/2}}$ and $E^{AlAs}_{As\ 3d_{5/2}}$ are the $3d_{5/2}$ CL BEs as-measured from the Ge and AlAs bulk-like surfaces, respectively, and E_{VBM} is the extracted valence band maximum (VBM) BE for each bulk-like material. Similarly, $E^{Ge}_{Ge\ 3d_{5/2}}(i)$ and $E^{AlAs}_{As\ 3d_{5/2}}(i)$ represent the $3d_{5/2}$ CL BEs as-measured from each respective material at the Ge/AlAs heterointerface (cf. Figures 6c and 6f).

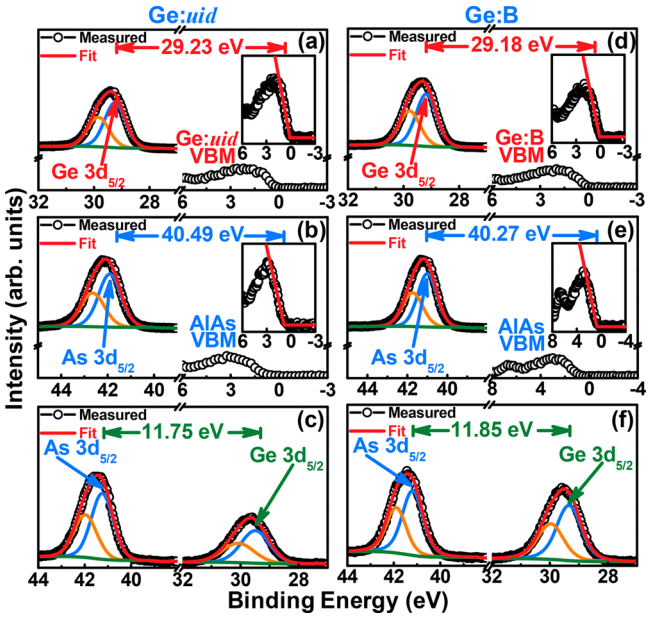

Figure 6. Representative XPS binding energy spectra of the (a−c) Ge:*uid*/AlAs(001) and (d−f) Ge:B/AlAs(001) heterostructures used in the determination of the empirical heterointerface valence and conduction band offsets. Panels a−c and d−f correspond to the bulk-like Ge (*uid* or B-doped) Ge 3d and valence band maximum, bulk-like AlAs As 3d and valence band maximum, and interfacial Ge 3d and As 3d core level spectra for the Ge:*uid* and Ge:B heterostructures, respectively.

E_{VBM} was determined by linearly fitting the onset of valence band photoemission from the background-subtracted XPS spectra in the vicinity of the Fermi edge. Following determination of the experimental ΔE_V, the heterointerfacial conduction band offset (ΔE_C) can be calculated using,

$$\Delta E_C = E^{AlAs}_g - \Delta E_V - E^{Ge}_g \quad (2)$$

where E^{AlAs}_g and E^{Ge}_g are the bandgap energies of AlAs and Ge, respectively. To ensure the highest-possible accuracy of the presented experimental results, the utilized Ge:B bandgap energy (0.64 eV) takes into account the slight reduction of the band edges due to strain, as calculated using deformation potential theory.[37]

Figure 7 graphically represents the experimentally derived flat-band energy band diagrams for the Ge:*uid*/AlAs(001) and Ge:B/AlAs(001) heterostructures, respectively. As can be found from Figure 7, the incorporation of B within the Ge epilayer resulted in an upward shift in the heterointerfacial ΔE^{XPS}_V, $\delta(\Delta E^{XPS}_V)$, of 0.26 eV. Accordingly, a downshift in ΔE^{XPS}_C, $\delta(\Delta E^{XPS}_C)$, of 0.23 eV was determined. The observed asymmetry in the shifts of the interfacial energy band discontinuities likely originates from the strain (ε_{Raman} = 0.29 ± 0.05%) applied to the Ge lattice via the incorporation of a high B concentration. As a result, both the Γ- and L-valley conduction band edges are lowered, whereas the splitting of the light-hole (upward in energy) and heavy-hole (downward in energy) valence bands lifts the valence band degeneracy. When combined with the change in the Ge quasi Fermi level due to B doping, the movement of the Ge band edges away

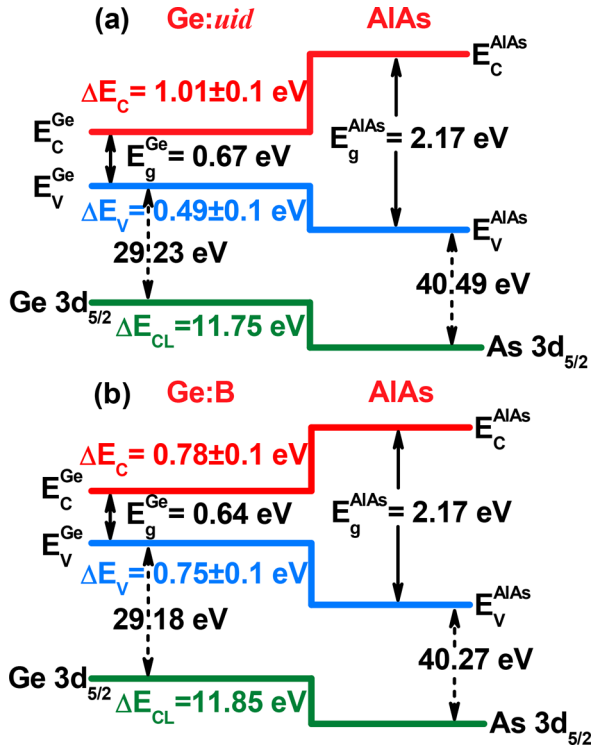

Figure 7. Experimentally determined electronic band structure at the (a) Ge:*uid*/AlAs(001) and (b) Ge:B/AlAs(001) heterointerfaces, respectively. A strained Ge bandgap value of 0.64 eV, calculated using our previously reported deformation potential framework,[37] was used in the band structure analysis of the Ge:B/AlAs(001) heterostructure.

DOI: 10.1021/acsaelm.9b00615
ACS Appl. Electron. Mater. 2019, 1, 2646−2654

Table 2. Calculated Shifts in 3d Semicore Energies with Associated Shifts in the Valence Band Offset, $\Delta E_V^{DFT}(3d)$, of Ge/AlAs(001) for As-Terminated AlAs[a]

	undoped Ge				B_{Ge} in ML1			
(-Ge-),(-As-)	$\Delta E_V^{DFT}(3d)$	$\delta(E_{int,Ge}(3d))$	$\delta(E_{int,As}(3d))$	$\delta(\Delta E_V^{DFT}(3d))$	$\Delta E_V^{DFT}(3d)$	$\delta(E_{Ge}(3d))$	$\delta(E_{As}(3d))$	$\delta(\Delta E_V^{DFT}(3d))$
(4Ge),(4Al)	0.78	0.00	0.00	0.00	1.02 (+0.24)	0.00	0.00	+0.24
(3Ge,1As),(4Al)	0.58	−0.20	0.00	−0.20	0.84 (+0.26)	−0.18	0.00	+0.06
(4Ge),(2Al,2Ge)	1.34	0.00	−0.56	+0.56	1.48 (+0.14)	0.00	−0.46	+0.70
(3Ge,1As,(2Al,2Ge)	1.14	−0.20	−0.56	+0.36	1.30 (+0.16)	−0.18	−0.46	+0.52
(2Ge,2As),(4Al)					0.52	−0.50	0.00	−0.26
(2Ge,2As),(2Al,2Ge)					0.99	−0.50	−0.46	+0.21
(3Ge,1B),(4Al)					1.06	+0.04	0.00	+0.28

[a]The (-Ge-),(-As-) column refers to nearest neighbors bonding to the Ge and As atoms near the interface, from which the contributions to $\Delta E_{int}(3d) = E_{int,Ge}(3d) - E_{int,As}(3d)$ are obtained. The shifts in averaged Ge (As) semicore level energies, $\delta(E_{int,Ge(As)}(3d))$, are relative to the semicore levels for ideal bonding in undoped and B-doped Ge. The shifts in valence band offsets, $\delta(\Delta E_V^{DFT}(3d))$, are relative to those of undoped Ge with ideal bonds (0.78 eV as calculated using DFT). For the case of B in ML1 (see text for definition), values in brackets denote changes in $\Delta E_V^{DFT}(3d)$ due to B doping, relative to the same nearest-neighbor bonding configuration. All units are in eV.

from their unstrained energy levels would be expected to give rise to the observed asymmetry in $\delta(\Delta E_V^{XPS})$ and $\delta(\Delta E_C^{XPS})$.

A more detailed investigation into the origin of the CL BE shifts observed in the experimental XPS spectra was performed by way of DFT calculations of the Ge/AlAs(001) heterointerface involving pseudopotentials which include the $n = 3$ orbital shell for As and Ge. The energies of these orbitals, relative to the valence band maximum, were then extracted and used to analyze the impact of heterointerface bonding configuration on the calculated valence band offset, $\Delta E_V^{DFT}(3d)$, as illustrated by Table 2. As shown in Table 2, nonoctet bonding of Ge and As, which could be expected to occur near the interface, has a significant impact on the relative energies of their respective 3d levels. In particular, taking the Ge contribution to $\Delta E_{int}(3d)$ from the average 3d energy of Ge atoms bonding to one As atom near the interface (with As remaining in its ideal bonding configuration) yields a peak Ge 3d orbital down-shifted 0.2 eV lower with respect to the ideal bonding configuration for Ge. This translates to a 0.2 eV decrease in $\Delta E_V^{DFT}(3d)$. Correspondingly, this has significant implications for the measured ΔE_V derived from XPS spectra, particularly in thinner samples in which interdiffused atoms within the vicinity of the heterointerface are likely to make a larger contribution to the measured spectral signal. Consequently, the local bonding configurations of heterovalent Ge:*uid*/AlAs(001) and Ge:B/AlAs(001) interfaces are expected to influence ΔE_V in physical (actual) systems.

These results therefore suggest that As atoms residing in Ge monolayers near the interface play a role in the determination of the heterointerfacial energy band structure. Comparing the band offsets calculated from eq 3 (see Materials and Methods) with the measured results presented in Figures 6 and 7, good agreement was found between the measured ΔE_V^{XPS} of 0.49 ± 0.1 eV and $\Delta E_V^{DFT}(3d)$ calculated supposing an interface consisting of Ge atoms with one of their four tetrahedral bonds coordinated with an As atom, i.e., $\Delta E_V^{DFT}(3d) = 0.58$ eV. Moreover, the likelihood of such an interface is buttressed by the As-rich conditions following III−V epitaxy, which would serve to increase the probability of interfacial Ge−As bond formation during Ge nucleation.

Focusing next on the heterointerface consisting of B-doped Ge, first-principles calculations show that placing a B atom in the Ge(001) monolayer, which bonds to the interfacial monolayer (referred to as "ML1" in Table 2), results in an increase in the potential within the Ge region. This increase in potential is accompanied by a corresponding increase in separation between Ge and As 3d orbital energies relative to the undoped case. As shown in Table 2, this results in an increase in $\Delta E_V^{DFT}(3d)$ of 0.14 eV − 0.26 eV when comparing a given nearest-neighbor bonding configuration for Ge and As atoms between the undoped and B-doped Ge systems. In particular, taking the average $E_{int,Ge}(3d)$ ($E_{int,As}(3d)$) from Ge bonding to one As atom and three Ge (four Al) atoms results in $\Delta E_V^{DFT}(3d) = 0.84$ eV, which is within 0.1 eV of the XPS-determined ΔE_V value, i.e., $\Delta E_V^{XPS} = 0.75$ eV, for the Ge:B/AlAs(001) system. The effect of B_{Ge} dopants near the interface on ΔE_V is summarized in Figure 8, in which $E_{int,Ge}(3d)$ is taken from Ge atoms with a range of local bonding configurations and then compared with the experimental results. As can be seen from Figure 8, the results of the first-principles modeling of the Ge/AlAs(001) heterointerface suggest that a slightly (two monolayer) diffuse $As_{0.25}Ge_{0.75}$ interlayer is most likely to form during growth, accordingly affecting the measured energy band structure at the interface,

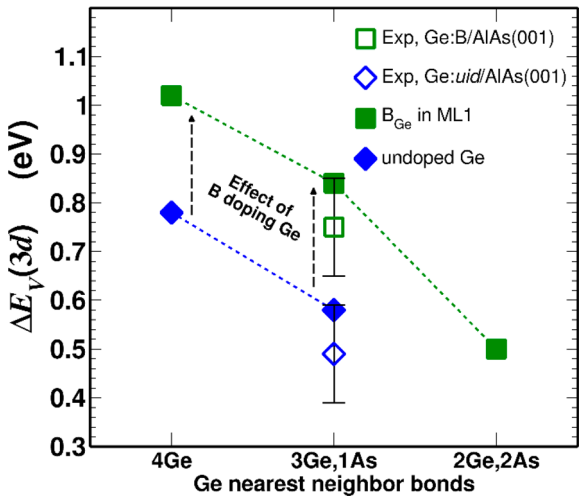

Figure 8. Valence band offsets, $\Delta E_V^{DFT}(3d)$, determined from the alignment of 3d orbital energies across the Ge/AlAs(001) interface (see Materials and Methods for additional details). The horizontal axis corresponds to different nearest-neighbor bonding configurations for Ge atoms near the interface. In all cases shown here, $E_{int}(3d)$ is taken from As atoms in their ideal bonding configuration (i.e., bonding to four Al atoms).

DOI: 10.1021/acsaelm.9b00615
ACS Appl. Electron. Mater. 2019, 1, 2646−2654

which is in excellent agreement with the ∼6 Å interdiffusion window observed at the Ge:B/AlAs heterointerface via APT analysis.

It is important to note that the effect of B dopants on ΔE_V will, in general, depend on B concentration. The local nature of the 3d orbitals allows for the use of computationally convenient simulation cells of relatively small dimensions parallel to the interface ((2 × 2) in units of the (110) lattice parameter) to model the interface and investigate the bonding dependence of 3d energies. However, this results in a correspondingly high simulated interfacial B density, with a B−B separation of approximately 8 Å. DFT calculations involving pseudopotentials which explicitly include only the outer valence electrons (Z = 3, 4, 5 for Al, Ge, and As, respectively) indicate a linear reduction in ΔE_V (calculated using the alignment of the electrostatic potential in bulk and interfacial simulation cells) as a function of increasing B−B separation. As the interfacial B density decreases, the Ge potential near the interface recovers its undoped value, such that extrapolating to zero B dopant concentration recovers the band offset of the Ge:*uid*/AlAs(001) system. Thus, the overestimation observed when comparing first-principles-calculated and experimental results could, at least partially, be explained by the high simulated B density (i.e., necessarily smaller simulation cells).

CONCLUSIONS

In summary, a joint experimental and theoretical approach was utilized to elucidate the formation of a 0.29 ± 0.05% biaxial tensile in-plane strain as a result of high B dopant incorporation ($N_B \approx 2-4 \times 10^{19}$ cm^{-3}) within Ge thin films. The impact of B incorporation on the energy band structure of Ge/AlAs(001) heterointerfaces was similarly systematically investigated, demonstrating an increase (decrease) in ΔE_V (ΔE_C) of 0.26 eV (0.23 eV), stemming from both the change in the Ge quasi Fermi level due to B doping as well as the strain introduced into the Ge lattice via substitutional B incorporation. First-principles DFT calculations of these interfaces were then utilized to determine the extent to which local (interfacial) bonding configuration influences the interfacial valence band offset, revealing a minimally diffuse interfacial region (approximately two monolayers in width) consisting of primarily Ge−As bonding. These results were independently corroborated via APT analysis, yielding an interfacial width (∼6 Å) in excellent agreement with the modeled interatomic diffusion window. This work thus provides a comprehensive understanding of the Ge:B/AlAs material system, thereby permitting its application toward emergent Ge-based electronic and photonic technologies.

MATERIALS AND METHODS

Materials Synthesis and Characterization. For this work, unintentionally (*uid*)- and B-doped epitaxial Ge thin films 270 and 290 nm thick were grown on 170 nm AlAs buffers grown on (001)GaAs substrates that were offcut by 2° and 6°, respectively, toward the ⟨110⟩ direction. Isolated III−V and Ge molecular beam epitaxy (MBE) chambers, connected *in situ* via an ultrahigh vacuum transfer chamber, were employed to minimize atomic interdiffusion at the Ge/AlAs interface. Prior to growth of the Ge/AlAs heterostructure, both substrates were desorbed of native Ga and As oxides at 750 °C under an As_2 overpressure of ∼1 × 10^{-5} Torr. Subsequently, a 0.25 μm GaAs homoepitaxial buffer was grown using a 650 °C growth temperature, after which the 0.17 μm AlAs large-bandgap buffer was immediately grown. The growth rates used in this work were 0.5 μm/h and 0.25 μm/h for the GaAs and AlAs epilayers, respectively. Following composite buffer growth, the substrates were gradually cooled (5 °C/min) to 150 °C and then transferred to the Ge growth chamber for Ge epitaxy. To this end, a low Ge growth temperature of 400 °C, and growth rate of ∼0.065 Å/s, were utilized to maintain smooth surface morphologies and limit cross-species contamination at the onset of and throughout the Ge growth. Solid-source, elemental B heated to 1650 °C in a high-temperature Knudsen cell was used as the B dopant source. In-situ reflection high-energy electron diffraction (RHEED) was used to monitor surface reconstruction and provide real-time feedback at all stages of growth.

High-resolution X-ray diffraction (HR-XRD) was used to investigate the impact of B doping on the structural properties of the Ge/AlAs/GaAs(001) heterostructures. For this purpose, triple-axis rocking curve measurements and reciprocal space mapping were performed using a PANalytical X-Pert Pro system equipped with a monochromated Cu Kα (λ = 1.540598 Å) X-ray source. Following the procedures outlined in ref 28, an experimental uncertainty of ±0.06% was ascribed to the XRD-derived strain-state of the Ge:B epilayer. Auxiliary, independent analysis of the Ge strain-state was performed using Raman spectra acquired in a (001) backscattering geometry via a JY Horiba LabRam HR800 system equipped with a 514.32 nm Ar laser excitation source. We note that an experimental uncertainty of ±0.05% was derived from the statistical deviation in the measured Ge:B longitudinal optical phonon mode peak position. To confirm the successful incorporation and activation of B within the as-grown Ge:B epilayer, Hall measurements utilizing the van der Pauw geometry were performed at 300 and 77 K, revealing a 2−4 × 10^{19} cm^{-3} carrier concentration exhibiting hole-like conduction. Similar measurements on the Ge:*uid* epilayer revealed a 2−4 × 10^{18} cm^{-3} carrier concentration exhibiting electron-like conduction, as previously reported.[22−25] The electronic band structure at the Ge/AlAs(001) heterointerface was characterized using a PHI Quantera SXM XPS system equipped with a monochromatic Al−Kα (E = 1486.7 eV) X-ray source. A low-energy electron flood gun was utilized during spectral acquisition to compensate for photogenerated electron loss and thereby minimize positive charge accumulation on the sample surface. We note that all XPS spectra were recorded using a pass energy of 26 eV and an exit angle of 45°. Fitting of the measured spectra was performed using CasaXPS v2.3.17 utilizing a Lorentzian convolution over a Shirley-type background and corrected with the adventitious carbon (C 1s) binding energy of 285.0 eV. An experimental uncertainty of ±0.04 eV was derived from the statistical deviation in the measured Au 4f$_{7/2}$ core level binding energy of a Au standard, wherein subsequent uncertainty was estimated using a root-sum-square approach. Lastly, investigation of the heterointerfacial abruptness between the Ge:B and AlAs epilayers was carried out via atom probe tomography (APT) analysis, which combines atomic projection imaging and time-of-flight spectroscopy to reconstruct atomically accurate three-dimensional (3-D) ion maps of selected volumes of material. The APT measurement conditions used in this work were optimized by cooling the sample to 50 K and reducing the laser pulse energy to 3 pJ at a pulse frequency of 250 kHz. An average detection rate of 0.01 ions/pulse was maintained through the analysis, which was performed parallel to the ⟨001⟩ growth direction. The commercially available IVAS software was used for the reconstruction of the 3-D ion maps presented herein.

First-Principles Calculations: Phonon Modes and Vibrational Properties. Atomistic density functional perturbation theory (DFPT)[39,40] calculations were performed to investigate the vibrational properties of bulk Ge in the presence of strain and B dopants. These simulations were carried out in the Quantum ESPRESSO software suite.[41] The local density approximation (LDA) to the exchange-correlation functional is used.[42] All pseudopotentials are generated from the norm-conserving Troullier−Martins method.[43] Bulk simulation cells and atomic coordinates are geometrically optimized using a 50 Ry kinetic energy cutoff with 72 (476) k-points used to sample the irreducible Brillouin zone for unstrained (biaxially strained) unit cells. For phonon dispersion curves, Γ-L and Γ-X directions were sampled with up to 50 q-points per direction, and a

DOI: 10.1021/acsaelm.9b00615
ACS Appl. Electron. Mater. 2019, 1, 2646−2654

total of 588 Monkhorst–Pack[44] k-points were used for summing over electronic eigenstates when calculating phonon dispersions for unstrained Ge. The reduced symmetry of biaxially strained Ge translates to denser k-point meshes of 3456 k-points for calculating phonon dispersions with similar accuracy as the unstrained case.

Simulation cells of increasing size (up to 216 atoms with xyz dimensions (3,3,3) in units of the (100) lattice constant) were used to calculate the dependence of the B_{Ge} local vibrational modes on B concentration in Ge. For the largest simulation cell (216 atoms), reciprocal space was sampled at the sole Γ point. Vibrational density of states were obtained using dynamical matrices calculated over grids of q-points selected to establish an optimal balance between numerical accuracy and computational cost for simulation cells of varying sizes. For example, a grid of 3 × 6 × 3 q-points was used for the dynamical matrix of the 32 atom B-doped simulation cell (with xyz dimensions (2,1,2) in units of the (100) lattice constant), while 6 × 6 × 6 q-points were used for the 8 atom (1,1,1) simulation cell.

First-Principles Calculations: Heterointerface Energy Band Discontinuity. A model of the interface consisting of nine Ge, nine AlAs (oriented in the (001) direction), and two mixed monolayers per interface was constructed to extract the semicore level energies near the interface. By employing pseudopotentials (PPs) which explicitly include the semicore $n = 3$ ($3s^2 3p^6 3d^{10}$) atomic shell for Ge (pseudoatomic number $Z = 22$) and As ($Z = 23$), the valence band discontinuity can be calculated by aligning the energies (relative to the valence band maximum) of the 3d levels in the respective bulk supercells ($E_{Ge,\,As}(3d)$), using their difference in energy across the interface ($\Delta E_{int}(3d)$),[45]

$$\Delta E_V = E_{Ge}(3d) - E_{As}(3d) + \Delta E_{int}(3d) \quad (3)$$

By taking contributions to $\Delta E_{int}(3d)$ from different atoms throughout the interface supercell, the effect of local bonding on the valence band offset (through its effect on the 3d level) can be investigated. Lastly, we note that all valence band offset calculations presented in this work follow the PP generation methodology and DFT exchange-correlation functional described earlier.

■ ASSOCIATED CONTENT

Supporting Information

The Supporting Information is available free of charge at https://pubs.acs.org/doi/10.1021/acsaelm.9b00615.

Graphical and qualitative outlines of the effect of B dopant incorporation on the local Ge–Ge bond length in the vicinity of B dopant atoms (PDF)

■ AUTHOR INFORMATION

Corresponding Author

*Tel.: (540) 231-6663; Fax: (540) 231-3362; E-mail: mantu.hudait@vt.edu.

ORCID

Michael B. Clavel: 0000-0002-2925-6099

Mantu K. Hudait: 0000-0002-9789-3081

Notes

The authors declare no competing financial interest.

■ ACKNOWLEDGMENTS

M.B.C. acknowledges partial support from the NSF under Grant ECCS-1507950, a US-Ireland joint R&D program. G.G.-D. and M.G. acknowledge the support of the Department for the Economy of Northern Ireland and InvestNI through the US-Ireland R&D partnership programme (No. USI-073). The authors also acknowledge the use of computational facilities at the Atomistic Simulation Centre—Queen's University Belfast. Lastly, the authors are grateful to the Institute for Critical Technology and Applied Science's Nanocharacterization and Fabrication Laboratory and Virginia Tech Nanofabrication for use of their characterization facilities.

■ REFERENCES

(1) Ouyang, Q.; Yang, M.; Holt, J.; Panda, S.; Chen, H.; Utomo, H.; Fischetti, M.; Rovedo, N.; Li, J.; Klymko, N.; Wildman, H.; Kanarsky, T.; Costrini, G.; Fried, D. M.; Bryant, A.; Ott, J. A.; Ieong, M.; Sung, C.-Y. Investigation of CMOS Devices with Embedded SiGe Source/Drain on Hybrid Orientation Substrates. *Int. Symp. VLSI Technol., Syst., Appl., Technol. Dig.* **2005**, 28.

(2) Yu, H.; Schaekers, M.; Hikavyy, A.; Rosseel, E.; Peter, A.; Hollar, K.; Khaja, F. A.; Aderhold, W.; Date, L.; Mayur, A. J.; Lee, J.-G.; Shin, K. M.; Douhard, B.; Chew, S. A.; Demuynck, S.; Kubicek, S.; Kim, D.; Mocuta, A.; Barla, K.; Horiguchi, N.; Collaert, N.; Thean, A. V.-Y.; De Meyer, K. Ultralow-Resistivity CMOS Contact Scheme with Pre-Contact Amorphization Plus Ti (Germano-)Silicidation. *Int. Symp. VLSI Technol., Syst., Appl., Technol. Dig.* **2016**, 1.

(3) Borland, J.; Lee, Y.-J.; Chuang, S.-S.; Tseng, T.-Y.; Liu, C.-W.; Huet, K.; Goodman, G.; Marino, J. Solid Solubility Limited Dopant Activation of Group III Dopants (B, Ga & In) in Ge Targeting sub-7nm Node Low p+ Contact Resistance. *Int. Workshop Junction Technol., 17th* **2017**, 94.

(4) Roth, J. E.; Fidaner, O.; Schaevitz, R. K.; Kuo, Y.-H.; Kamins, T. I.; Harris, J. S.; Miller, D. A. B. Optical Modulator on Silicon Employing Germanium Quantum Wells. *Opt. Express* **2007**, *15*, 5851–5859.

(5) Oehme, M.; Gollhofer, M.; Widmann, D.; Schmid, M.; Kaschel, M.; Kasper, E.; Schulze, J. Direct Bandgap Narrowing in Ge LED's on Si Substrates. *Opt. Express* **2013**, *21*, 2206–2211.

(6) Kasper, E.; Oehme, M.; Arguirov, T.; Werner, J.; Kittler, M.; Schulze, J. Room Temperature Direct Band Gap Emission from Ge p-i-n Heterojunction Photodiodes. *Adv. OptoElectron.* **2012**, *2012*, 1–4.

(7) Gallacher, K.; Velha, P.; Paul, D. J.; Cecchi, S.; Frigerio, J.; Chrastina, D.; Isella, G. 1.55 μm Direct Bandgap Electroluminescence from Strained n-Ge Quantum Wells Grown on Si Substrates. *Appl. Phys. Lett.* **2012**, *101*, 211101.

(8) Newton, P. J.; Llandro, J.; Mansell, R.; Holmes, S. N.; Morrison, C.; Foronda, J.; Myronov, M.; Leadley, D. R.; Barnes, C. H. W. Magnetotransport in p-type Ge Quantum Well Narrow Wire Arrays. *Appl. Phys. Lett.* **2015**, *106*, 172102.

(9) Zhou, Y.; Han, W.; Chang, L.-T.; Xiu, F.; Wang, M.; Oehme, M.; Fischer, I. A.; Schulze, J.; Kawakami, R. K.; Wang, K. L. Electrical Spin Injection and Transport in Germanium. *Phys. Rev. B: Condens. Matter Mater. Phys.* **2011**, *84*, 125323.

(10) Aubin, J.; Hartmann, J. M.; Veillerot, M.; Essa, Z.; Sermage, B. Very Low Temperature (450°C) Selective Epitaxial Growth of Heavily *in situ* Boron-Doped SiGe Layers. *Semicond. Sci. Technol.* **2015**, *30*, 115006.

(11) Uppal, S.; Willoughby, A. F. W.; Bonar, J. M.; Evans, A. G. R.; Cowern, N. E. B.; Morris, R.; Dowsett, M. G. Diffusion of Ion-Implanted Boron in Germanium. *J. Appl. Phys.* **2001**, *90*, 4293–4295.

(12) Chang, T.-H.; Chang, C.; Chu, Y.-H.; Lee, C.-C.; Chang, J.-Y.; Chen, I.-C.; Li, T. Low Temperature Growth of Highly Conductive Boron-Doped Germanium Thin Films by Electron Cyclotron Resonance Chemical Vapor Deposition. *Thin Solid Films* **2014**, *551*, 53–56.

(13) Han, B.; Shimizu, Y.; Wipakorn, J.; Nishibe, K.; Tu, Y.; Inoue, K.; Fukata, N.; Nagai, Y. Boron Distributions in Individual Core-Shell Ge/Si and Si/Ge Heterostructured Nanowires. *Nanoscale* **2016**, *8*, 19811–19815.

(14) Bogumilowicz, Y.; Hartmann, J. M. Reduced-Pressure Chemical Vapor Deposition of Boron-Doped Si and Ge Layers. *Thin Solid Films* **2014**, *557*, 4–9.

(15) Kuo, W.-C.; Lee, M. J.; Wu, M.-L.; Lee, C.-C.; Tsao, I.-Y.; Chang, J.-Y. Low Temperature Growth of Heavily Boron-Doped Hydrogenated Ge Epilayers and its Application in Ge/Si Photodetectors. *Solid-State Electron.* **2017**, *130*, 41–44.

(16) Satta, A.; Simoen, E.; Clarysse, T.; Janssens, T.; Benedetti, A.; De Jaeger, B.; Meuris, M.; Vandervorst, W. Diffusion, Activation, and

DOI: 10.1021/acsaelm.9b00615
ACS Appl. Electron. Mater. 2019, 1, 2646–2654

Recrystallization of Boron Implanted in Preamorphized and Crystalline Germanium. *Appl. Phys. Lett.* **2005**, *87*, 172109.
(17) Hutin, L.; Koffel, S.; Le Royer, C.; Clavelier, L.; Scheiblin, P.; Mazzocchi, V.; Deleonibus, S. Activation Level in Boron-Doped Thin Germanium-on-Insulator (GeOI): Extraction Method and Impact of Mobility. *Mater. Sci. Semicond. Process.* **2008**, *11*, 267−270.
(18) Jung, W.-S.; Nam, J. H.; Pal, A.; Lee, J. H.; Na, Y.; Kim, Y.; Lee, J. H.; Saraswat, K. C. Reduction of Surface Roughness in Epitaxially Grown Germanium by Controlled Thermal Oxidation. *IEEE Electron Device Lett.* **2015**, *36*, 297−299.
(19) Chau, R.; Doyle, B.; Datta, S.; Kavalieros, J.; Zhang, K. Integrated Nanoelectronics for the Future. *Nat. Mater.* **2007**, *6*, 810−812.
(20) Hutin, L.; Le Royer, C.; Damlencourt, J.-F.; Hartmann, J.-M.; Grampeix, H.; Mazzocchi, V.; Tabone, C.; Previtali, B.; Pouydebasque, A.; Vinet, M.; Faynot, O. GeOI pMOSFETs Scaled Down to 30-nm Gate Length with Record Off-State Current. *IEEE Electron Device Lett.* **2010**, *31*, 234−236.
(21) Letertre, F.; Deguet, C.; Richtarch, C.; Faure, B.; Hartmann, J. M.; Chieu, F.; Beaumont, A.; Dechamp, J.; Morales, C.; Allibert, F.; Perreau, P.; Pocas, S.; Personnic, S.; Lagahe-Blanchard, C.; Ghyselen, B.; Le Vaillant, Y. M.; Jalaguier; Kernevez, N.; Mazure, C. Germanium-on-Insulator (GeOI) Structure Realized by the Smart Cut Technology. *Mater. Res. Soc. Symp. Proc.* **2004**, *809*, B4.4.1−B4.4.6.
(22) Hudait, M. K.; Clavel, M.; Goley, P.; Jain, N.; Zhu, Y. Heterogeneous Integration of Epitaxial Ge on Si using AlAs/GaAs Buffer Architecture: Suitability for Low-Power Fin Field-Effect Transistors. *Sci. Rep.* **2015**, *4*. DOI: 10.1038/srep06964
(23) Nguyen, P. D.; Clavel, M. B.; Goley, P. S.; Liu, J.-S.; Allen, N. P.; Guido, L. J.; Hudait, M. K. Heteroepitaxial Ge MOS Devices on Si Using Composite AlAs/GaAs Buffer. *IEEE J. Electron Devices Soc.* **2015**, *3*, 341−348.
(24) Nguyen, P. D.; Clavel, M. B.; Ghosh, A.; Hudait, M. K. Metal Work Function Engineering on Epitaxial (100)Ge and (110)Ge Metal-Oxide-Semiconductor Devices. *Microelectron. Eng.* **2018**, *199*, 80−86.
(25) Nguyen, P. D.; Clavel, M. B.; Liu, J.-S.; Hudait, M. K. Investigating FinFET Sidewall Passivation Using Epitaxial (100)Ge and (110)Ge Metal-Oxide-Semiconductor Devices on AlAs/GaAs. *IEEE Trans. Electron Devices* **2017**, *64*, 4457−4465.
(26) Pavarelli, N.; Ochalski, T. J.; Murphy-Armando, F.; Huo, Y.; Schmidt, M.; Huyet, G.; Harris, J. S. Optical Emission of a Strained Direct-Band-Gap Ge Quantum Well Embedded Inside InGaAs Alloy Layers. *Phys. Rev. Lett.* **2013**, *110*, 177404.
(27) Clavel, M.; Goley, P.; Jain, N.; Zhu, Y.; Hudait, M. K. Strain-Engineered Biaxial Tensile Epitaxial Germanium for High-Performance Ge/InGaAs Tunnel Field-Effect Transistors. *IEEE J. Electron Devices Soc.* **2015**, *3*, 184−193.
(28) Clavel, M.; Saladukha, D.; Goley, P. S.; Ochalski, T. J.; Murphy-Armando, F.; Bodnar, R. J.; Hudait, M. K. Heterogeneously-Grown Tunable Tensile Strained Germanium on Silicon for Photonic Devices. *ACS Appl. Mater. Interfaces* **2015**, *7*, 26470−26481.
(29) Hudait, M. K.; Lin, Y.; Ringel, S. A. Strain Relaxation Properties of $InAs_yP_{1-y}$ Metamorphic Materials Grown on InP Substrates. *J. Appl. Phys.* **2009**, *105*, 061643.
(30) Chauveau, J.-M.; Androussi, Y.; Lefebvre, A.; Di Persio, J.; Cordier, Y. Indium Content Measurements in Metamorphic High Electron Mobility Transistor Structures by Combination of X-ray Reciprocal Space Mapping and Transmission Electron Microscopy. *J. Appl. Phys.* **2003**, *93*, 4219−4225.
(31) Madelung, O. *Semiconductors: Intrinsic Properties of Group IV Elements and III-V, II-VI, and I-VII Compounds*, Vol. *22a*; Springer: Berlin, 1985.
(32) Lu, X.; Jiang, Z.; Zhu, H.; Zhang, X.; Wang, X. Observation of Boron Doping Induced Surface Roughening in Silicon Molecular Beam Epitaxy. *Appl. Phys. Lett.* **1996**, *68*, 3278−3280.
(33) People, R.; Bean, J. C. Calculation of Critical Layer Thickness versus Lattice Mismatch for Ge_xSi_{1-x}/Si Strained-Layer Heterostructures. *Appl. Phys. Lett.* **1985**, *47*, 322−324.
(34) Bai, Y.; Lee, K. E.; Cheng, C.; Lee, M. L.; Fitzgerald, E. A. Growth of Highly Tensile-Strained Ge on Relaxed $In_xGa_{1-x}As$ by Metal Organic Chemical Vapor Deposition. *J. Appl. Phys.* **2008**, *104*, 084518.
(35) Fang, Y.-Y.; Tolle, J.; Roucka, R.; Chizmeshya, A. V. G.; Kouvetakis, J.; D'Costa, V. R.; Menéndez, J. Perfectly Tetragonal, Tensile-Strained Ge on $Ge_{1-y}Sn_y$ Buffered Si(100). *Appl. Phys. Lett.* **2007**, *90*, 061915.
(36) Sanson, A.; Napolitani, E.; Carnera, A.; Impellizzeri, G.; Giarola, M.; Mariotto, G. A Non-Destructive Approach for Doping Profiles Characterization by Micro-Raman Spectroscopy: The Case of B-Implanted Ge. *J. Raman Spectrosc.* **2014**, *45*, 197−201.
(37) Clavel, M. B.; Hudait, M. K. Band Offset Enhancement of a-Al_2O_3/Tensile-Ge for High Mobility Nanoscale pMOS Devices. *IEEE Electron Device Lett.* **2017**, *38*, 1196−1199.
(38) Kraut, E. A.; Grant, R. W.; Waldrop, J. R.; Kowalczyk, S. P. Precise Determination of the Valence-Band Edge in X-ray Photoemission Spectra: Application to Measurement of Semiconductor Interface Potentials. *Phys. Rev. Lett.* **1980**, *44*, 1620−1623.
(39) Giannozzi, P.; de Gironcoli, S.; Pavone, P.; Baroni, S. Ab Initio Calculation of Phonon Dispersions in Semiconductors. *Phys. Rev. B: Condens. Matter Mater. Phys.* **1991**, *43*, 7231−7242.
(40) Baroni, S.; de Gironcoli, S.; Dal Corso, A.; Giannozzi, P. Phonons and Related Crystal Properties from Density-Functional Perturbation Theory. *Rev. Mod. Phys.* **2001**, *73*, 515−562.
(41) Giannozzi, P.; Baroni, S.; Bonini, N.; Calandra, M.; Car, R.; Cavazzoni, C.; Ceresoli, D.; Chiarotti, G. L.; Cococcioni, M.; Dabo, I.; Dal Corso, A.; de Gironcoli, S.; Fabris, S.; Fratesi, G.; Gebauer, R.; Gerstmann, U.; Gougoussis, C.; Kokalj, A.; Lazzeri, M.; Martin-Samos, L.; Marzari, N.; Mauri, F.; Mazzarello, R.; Paolini, S.; Pasquarello, A.; Paulatto, L.; Sbraccia, C.; Scandolo, S.; Sclauzero, G.; Seitsonen, A. P.; Smogunov, A.; Umari, P.; Wentzcovitch, R. M. Quantum Espresso: A Modular and Open-Source Software Project for Quantum Simulations of Materials. *J. Phys.: Condens. Matter* **2009**, *21*, 395502.
(42) Perdew, J. P.; Wang, Y. Accurate and Simple Analytic Representation of the Electron-Gas Correlation Energy. *Phys. Rev. B: Condens. Matter Mater. Phys.* **1992**, *45*, 13244−13249.
(43) Troullier, N.; Martins, J. L. Efficient Pseudopotentials for Plane-Wave Calculations. *Phys. Rev. B: Condens. Matter Mater. Phys.* **1991**, *43*, 1993−2006.
(44) Monkhorst, H. J.; Pack, J. D. Special Points for Brillouin-Zone Integrations. *Phys. Rev. B* **1976**, *13*, 5188−5192.
(45) Wei, S. H.; Zunger, A. Calculated Natural Band Offsets of all II-VI and III-V Semiconductors: Chemical Trends and the Role of Cation *d* Orbitals. *Appl. Phys. Lett.* **1998**, *72*, 2011−2013.

DOI: 10.1021/acsaelm.9b00615
ACS Appl. Electron. Mater. 2019, 1, 2646−2654